Remote Sensing of Environment 112 (2008) 4148–4158

Contents lists available at ScienceDirect

Remote Sensing of Environment

journal homepage: www.elsevier.com/locate/rse

# Surface hydrology of low-relief landscapes: Assessing surface water flow impedance using LIDAR-derived digital elevation models

Krista L. Jones [a,*], Geoffrey C. Poole [a,b,c], Scott J. O'Daniel [d,e], Leal A.K. Mertes [e,1], Jack A. Stanford [c]

[a] Eco-metrics, Inc. 2520 Pine Lake Road, Tucker, GA 30084, United States
[b] Institute of Ecology, University of Georgia, Athens, GA 30602, United States
[c] Flathead Lake Biological Station, University of Montana, Polson, MT 59860, United States
[d] Confederated Tribes of the Umatilla Indian Reservation, PO Box 638, Pendleton, OR 97801, United States
[e] Geography Department, University of California at Santa Barbara, Santa Barbara, CA 93106, United States

ARTICLE INFO

*Article history:*
Received 3 April 2007
Received in revised form 31 December 2007
Accepted 12 January 2008

*Keywords:*
Hydrologic modeling
Flooding
Geomorphology
Floodplain connectivity
Laser altimetry
Link-and-node network
Umatilla River Floodplain, Oregon

ABSTRACT

Conventional hydrologic analyses of digital elevation models (DEMs) perform well in areas of high topographic relief, where surface water flow is typically unidirectional, convergent, spatially static, and directed toward a single discharge point at the edge of a catchment. Such analyses do not perform well on landscapes with low topographic relief (e.g., floodplains, river deltas, coastal wetlands, and estuaries) where surface water flow is influenced by subtle topographic depressions and may be bidirectional, divergent, and spatially dynamic in response to hydrologic forcing such as tides or variation in river discharge. We developed a framework for hydrologic analysis of low-relief landscapes using a high-resolution (1 m) DEM derived from light detection and ranging (LIDAR) data collected over a ~8.8 km$^2$ section of the Umatilla River Floodplain, Oregon, USA. Our approach assessed the pattern and characteristics of "hydrologic facets" (landscape patches that have high internal surface water connectivity and therefore function as a single hydrologic unit), where facet boundaries were defined by subtle topographic divides across the floodplain. We initially identified nearly 6000 small (fine-scale) hydrologic facets using standard GIS processing algorithms. We located the divide between each pair of adjacent facets, and determined "hydrologic impedance" (i.e., the maximum change in river stage necessary to inundate the divide) for each divide ($n$ = ~17,000). Using hydrologic impedance values, we analyzed patterns of surface water connectivity among the fine-scale facets and aggregated groups of adjacent facets that had high connectivity. This process yielded a reduced number of larger facets useful for hydrologic analysis at coarser spatial scales. We compared results derived using several alternate rule sets for aggregating facets. With appropriate aggregation rules, the results are useful for generating optimal link-and-node flow networks to support hydrologic modeling of surface water flux across low-relief landscapes.



## 1. Introduction

Widely applied techniques for hydrologic analysis of digital elevation models (DEMs) (Jenson & Domingue, 1988; Jenson, 1991) often treat internally draining depressions ("sinks") in a DEM as data imperfections which are filled to prevent flow paths from terminating within depressions (sensu Maidment, 2002; Wang & Liu, 2006). On resulting filled DEMs, water flow is generally convergent and unidirectional (i.e. water moves from high to low elevation). Thus, flowpaths from adjacent hillslopes converge to form channels, channels converge to form stream networks, and water from any point in a drainage basin flows toward a point of discharge at the edge of the catchment. While this approach works well for landscapes with high topographic relief, it is less applicable to low-relief fluvial landscapes such as floodplains, coastal wetlands, and estuaries (Lohani & Mason, 2001). In fact, state-of-the-art algorithms for extracting channel networks from remote sensing data for low-relief landscapes (e.g., Mason et al., 2006) are neither straightforward nor widely standardized.

The hydrology of low-relief landscapes is fundamentally different from that of high-relief landscapes because water depths on low-relief landscapes periodically exceed much of the range in topographic variation. Thus, on low-relief landscapes, subtle elevation gradients influence ecological and hydrologic dynamics such as vegetation patterns (Fonda, 1974; Malanson & Butler, 1991; Byrd & Kelly, 2006; Gurnell et al., 2006), habitat diversity (Zedler et al., 1999; Florsheim & Mount, 2002; Lorang et al., 2005), and surface water "connectivity" (Poole et al., 2002); see Pringle (2003a) for a general discussion of hydrologic connectivity). Contrary to the conventional hydrologic

* Corresponding author. Tel.: +1 770 621 0266; fax: +1 770 270 1994.
*E-mail address:* krista.lee.jones@gmail.com (K.L. Jones).
[1] Posthumous publication.

0034-4257/$ – see front matter © 2008 Elsevier Inc. All rights reserved.
doi:10.1016/j.rse.2008.01.024

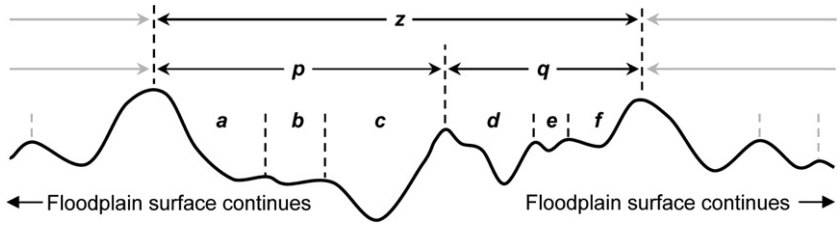


**Fig. 1.** Hypothetical fragment of a floodplain cross-sectional elevation profile illustrating the hierarchy of hydrologic facets across spatial scales. For hydrologic analysis at fine spatial scales, each depression (*a–f*) might be considered a distinct hydrologic facet. At an intermediate scale, minor divides could be ignored, allowing *a–c* and *d–f* to be merged, yielding two facets, *p* and *q*. Finally, for a coarse-scale analysis, all but the most substantive divides could be ignored, and depressions *a–f* might be represented as a single hydrologic facet, *z*.

analysis of DEMs, surface water flux on low-relief landscapes may be bidirectional (e.g., tides force water from lower elevations to higher elevation), divergent (e.g., braided rivers, river deltas), and influenced markedly by topographic depressions (e.g., instream pools, floodplain ponds, tide pools). Additionally, variation in river discharge, such as seasonal flood spates, can activate lateral surface water connections among channels and their associated floodplains, creating flow networks that expand and contract laterally (Junk et al., 1989; Malard et al., 1999). Therefore, a conceptual framework for assessing hydrologic interactions on low-relief landscapes must allow for bidirectional flow, divergent flow paths, and dynamic topology within a hydrologic network.

Assessing the subtle geomorphic features of low-relief landscapes requires DEMs with higher horizontal and vertical resolution than the 30-m or 10-m DEMs widely available. DEMs derived from light detection and ranging (LIDAR) have sufficient resolution, e.g., <1 m grids; +/−10 cm vertical accuracy (Lane et al., 2003), to capture topographic gradients that control surface water hydrology across low-relief landscapes (Casas et al., 2006). These detailed DEMs, however, may contain more information than is required (or even useful) for some applications. In such cases, it is advantageous to simplify the data to create a more manageable topographic representation of the landscape. One common approach is to create a DEM with coarser resolution, which may obfuscate geomorphic features on low-relief landscapes (Woolard & Colby, 2002). More sophisticated data filtering approaches reduce LIDAR data density by identifying points that represent the location of local minima and maxima and significant slope breaks (see discussion in Bates et al., 2003; Omer et al., 2003). As an alternative, we demonstrate how high-resolution DEMs derived from LIDAR can be simplified by aggregating pixels into irregularly-shaped hydrologic facets (i.e., landscape patches that have high internal surface water connectivity and therefore can be considered a single hydrologic unit) bounded by channel banks, terrace edges, gravel-bar crests, and other topographic divides that ultimately control surface water flow. We demonstrate how these facets can be used to assess spatial patterns of surface water flow impedance across low-relief landscapes, and illustrate how such an analysis is useful for parameterizing a finite volume hydrologic network model to simulate dynamic water flux across a floodplain surface.

### 1.1. Conceptual framework

Low-relief fluvial landscapes are the legacy of alternating depositional and erosional processes that create a complicated ridge and swale topography (Leopold et al., 1964) where surface water flow paths are not always immediately apparent (e.g., across unchannelized portions of a floodplain). In order to assess such surface water flow paths, we conceptualize these landscapes as a collection of depressions rather like an egg carton, but where the depressions are irregularly shaped, have varying depths, and are separated by divides of varying heights. This analogy for fluvial landscapes may seem counterintuitive unless channel features like pool-riffle sequences are recognized as streambed depressions (pools) separated by divides (riffles) despite the fact they are typically submerged. Surface water begins to flow between two adjacent depressions when water stage (the elevation of the water surface) exceeds the elevation of the interceding hydrologic divide. Using this framework, our analysis identifies "hydrologic facets," or collections of adjacent and hydrologically well-connected depressions. Because depressions contained within a facet are well-connected, a hydrologic facet can be viewed as a single, functional hydrologic unit of the landscape. Facets exist within a hierarchy; several facets identified at a fine spatial scale can be merged to yield a facet suitable for assessments at coarser spatial scales (Fig. 1). Because facet boundaries follow topographic divides, they trace the geomorphic controls on surface water flux across the landscape.

Given an accurate DEM of a low-relief landscape, patterns of hydrologic connection across the landscape can be approximated simply by using a map of landscape elevation relative to the adjacent water stage in the river (sensu Townsend & Walsh, 1998; Lorang et al., 2005). In contrast, a process for extracting a single set of facets and

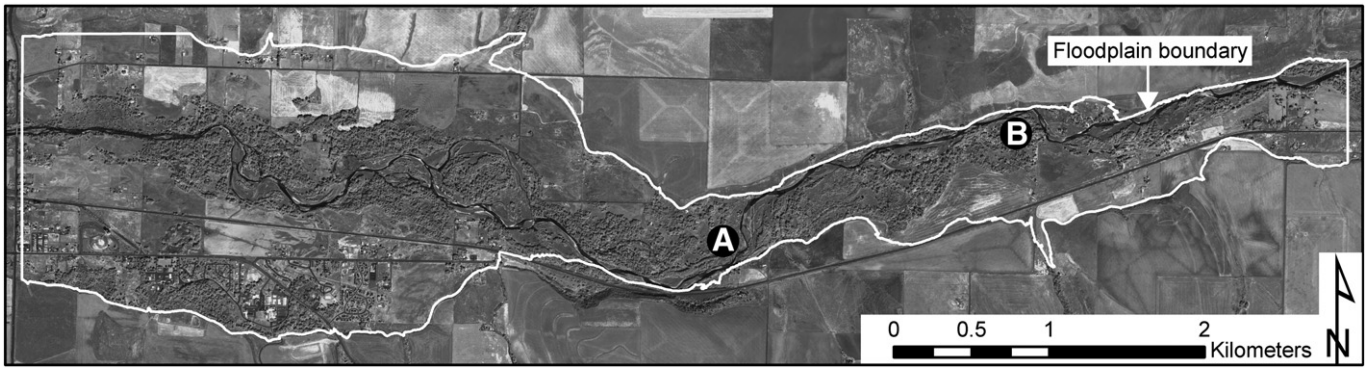


**Fig. 2.** Quickbird imagery (collected on 7/4/2004 by Satellite Imaging Corporation, Houston, TX) of the Umatilla River Floodplain study site in northeastern Oregon, USA. Study site area denoted by white boundary. A water surface elevation profile from point *b* to *a* is shown in Fig. 6.

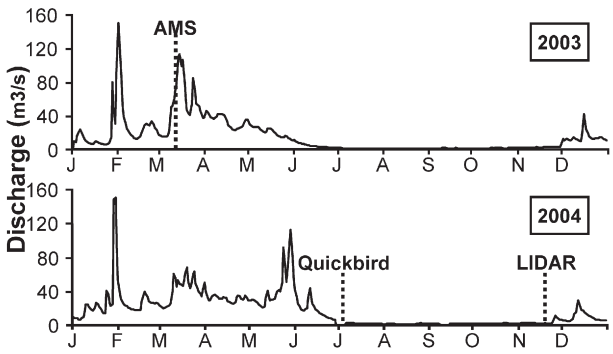


**Fig. 3.** Discharge data ($m^3/s$) from 2003 and 2004 for the main channel Umatilla River (US Geological Survey "Umatilla River at West Reservation Boundary Near Pendleton, OR" gauge, located ~9.5 km downstream from the study site). Dates of remote sensing data collection are indicated on the hydrographs.

divides from a DEM in order to assess patterns of surface water flux for a range of water stages is somewhat less obvious. An optimized solution to this problem would identify a configuration of facets that are bounded by divides with the highest "hydrologic impedance" across the floodplain, where high impedance signifies low surface water connectivity (sensu Pringle, 2003b; Kondolf et al., 2006) between adjacent facets. To be most useful, this type of analysis would operate at any spatial scale by allowing the user to control the average spatial extent of facets identified by the analysis.

Combined, the concepts of hydrologic facets, divides, and impedance form the basis of an optimization approach we developed to simplify an initial configuration of fine-scale (small) facets into coarser-scale (larger) facets. The approach strategically dissolves divides with low hydrologic impedance, thus merging adjacent facets with high hydrologic connectivity. We demonstrate our technique by determining the optimal representation of facets and divides at several spatial scales, derived using three different impedance thresholds below which divides are dissolved.

## 2. Study site

Our study site is an 8.8 $km^2$ section of Umatilla River Floodplain (Fig. 2) on the Umatilla Indian Reservation near the town of Pendleton in northeastern Oregon, USA. Set within the high desert, the Umatilla River ultimately drains into the Columbia River near the town of Hermiston. The river flows east-to-west at our study site, which is upstream of the significant agricultural water withdrawals common in the lower section of the river. Unaffected by dams, much of the floodplain maintains the naturally anabranched (coarsely braided) channel pattern typical of free-flowing alluvial rivers in much of the western U.S. Precipitation occurs typically in winter or spring, as rain on the floodplain (0.3 m/year) and as rain or snow in the surrounding Blue Mountains (0.8 to 1.8 m/year) (U.S. National Oceanographic and Atmospheric Administration climate data). Long-term discharge data recorded by the U.S. Geological Survey show that the Umatilla River discharge is ~1 $m^3/s$ at baseflow and 85 $m^3/s$ at bank-full (1.5 year return interval) flows (USGS gauge "Umatilla River at Pendleton, OR," ID = 14021000, period of record: 1904–1989, located ~8 km downstream of our site). Typical seasonal freshets result from spring-time snowmelt or rain-on-snow events in the Blue Mountains east of our study site. Discharge during 2003 and 2004, the years of remote sensing data collection for this study, were similar to long-term conditions (Fig. 3) (USGS gauge "Umatilla River at West Reservation Boundary near Pendleton, OR," ID = 14020850, period of record: 1997–present, located ~3 km downstream of our site).

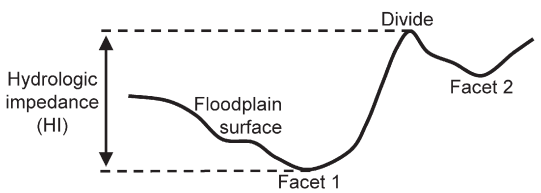


**Fig. 4.** Hypothetical example of a hydrologic divide separating adjacent facets. Hydrologic impedance (HI) quantifies the maximum change in stage required to inundate the divide.

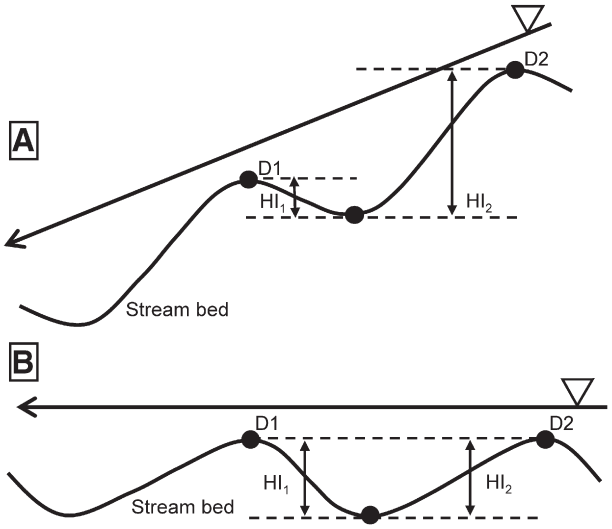


**Fig. 5.** Downstream slope in a river's water surface can impart bias in calculation of hydrologic impedance (HI). (A) Although the same change in stage inundates the divides (D1 and D2), the water surface tilt results in $HI_1 < HI_2$. (B) Detrending the floodplain's elevation relative to river stage results in correct HI calculations so that $HI_1 = HI_2$.

At the site, the floodplain is confined by bedrock valley walls and varies in width from ~0.5 km wide at the upstream, eastern end, narrowing to ~0.3 km, and then expanding again to ~1.6 km at the downstream, western end (Fig. 2). At baseflow, the main channel frequently divides into multiple channels and then re-converges. Common geomorphic features include mid-channel and lateral bars and small spring channels (10–100 m in length) within the bank-full scour zone. At bank-full flow, these multiple channels merge into a single main channel. However, bank-full flows activate lateral flood channels which are inactive during baseflow, creating a new coarser-scale pattern of channel braiding on the floodplain. Additional information about the geomorphology, hydrology, and hydrogeology of this Umatilla River floodplain can be found in Jones et al. (2008).

## 3. Methods

### 3.1. Quantifying hydrologic impedance

Conceptually, hydrologic impedance is a characteristic of the divide between any two adjacent hydrologic facets on the floodplain; adjacent facets have high surface water connectivity if the divide separating them has low impedance. To be useful for assessing surface water connectivity across a range of river stages, any measure of hydrologic impedance must be independent of water stage. We propose that hydrologic impedance of a divide can be defined as the difference between: 1) the minimum elevation along the divide; and 2) the lesser of the minimum elevations of the two associated facets:

$$\mathrm{HI} = \mathrm{MinDivE} - Min(DepE_1, DepE_2) \quad (1)$$

where

| | |
|---|---|
| HI | hydrologic impedance |
| MinDivE | minimum elevation along a divide |
| $DepE_x$ | elevation of lowest point in facet $x$ |

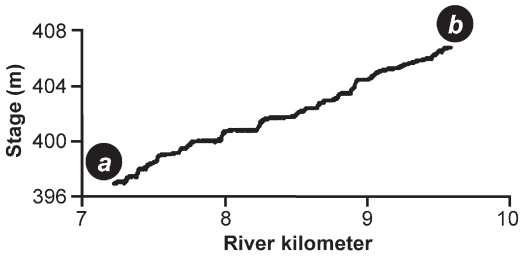


**Fig. 6.** Longitudinal water surface profile for a 2 km section of river bounded by points *a* and *b* in Fig. 2.

In concept, HI quantifies the maximum change in water stage that would be required to initiate surface water flow across a divide separating two facets (Fig. 4). Thus, a boundary has high hydrologic impedance when a large change in river stage is required to create a surface water connection between the facets separated by the boundary.

### 3.2. LIDAR processing

#### 3.2.1. Generating the DEM

A commercial contractor collected LIDAR data for our study site during low flow conditions (river surface elevation=0.83 m gauge height at the USGS West Reservation Boundary gauge) on November 20 and 21, 2004 (Fig. 3) using an Optech ALTM 3100 airborne laser terrain mapper. The instrument was set to a 50 kHz laser repetition rate and flown at 1100 m AGL, capturing a 40° scan width (20° from NADIR) and yielding an average sampling density >4 points per $m^2$. To construct a DEM of the ground surface, we used TerraModeler software (marketed by TerraSolid) to extract the bare earth echoes from the raw LIDAR data, create TINs, and output ARCINFO ASCII lattice models. These lattice models were imported into ArcGIS 9.1 (ERSI, Redlands, CA) and resampled to 1-m resolution grids. Based on a comparison of laser points to 306 real-time kinematic (RTK) ground level survey points, root mean square error (RMSE) of the final DEM was 0.54 m in the horizontal plane and 0.04 m vertically.

The resulting "wet-floodplain" DEM surface included the elevation of the baseflow water surface anywhere the floodplain was inundated, which imparts errors in LIDAR representations of channel cross sections (Charlton et al., 2003). To create a "dry-floodplain" DEM that incorporated the streambed bathymetry (i.e., the streambed elevation rather than the baseflow water surface elevation), we subtracted a spatially continuous representation of water depth from the wet-floodplain DEM. We derived this water depth grid from satellite Quickbird data (Satellite Imaging Corporation, Houston, TX) collected on 7/4/2004 at flow conditions (river surface elevation=0.85 m gauge height) similar to the LIDAR overflight (0.83 m gauge height) (Fig. 3). The digital numbers (DN) of the Quickbird data were converted to at-sensor radiances (L) using published calibration constants for all 4 Quickbird bands (Space Imaging Corporation, 2004). Then, we sharpened the multispectral Quickbird data using the panchromatic band from the same dataset. This was accomplished using the Gramm–Schmidt orthoganilisation where a simulated panchromatic band was created by calculating the average brightness from each of the multispectral bands and taking the ratio of the brightness of the pan to multispectral bands in a pair wise manner. Next, the initial simulated panchromatic band was substituted for the first multispectral band. This process was repeated for each of the 4 multispectral bands. Then, the inverse of the Gramm–Schmidt orthoganilisation was applied to the entire simulated multispectral image to produce a final pan-sharpened image. We used this final image to estimate water depth because its increased spatial resolution enabled differentiation of instream depths.

To derived a baseflow water mask, we performed a supervised classification of green (0.52–0.60 µm), blue (0.45–0.52 µm), and near infrared (0.76–0.90 µm) bands from the processed Quickbird data on a ~40 km section of the river, which included our study site. Occasionally, shadows were misclassified as water. These shadows

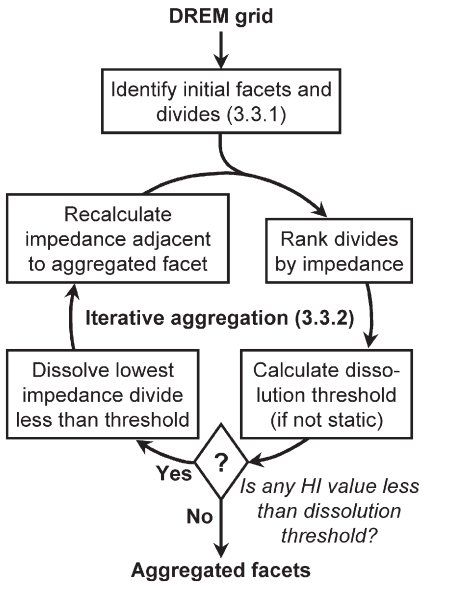


**Fig. 7.** Workflow for creating an optimal distribution of floodplain facets based on hydrologic impedance from a digital relative elevation model (DREM, described in Section 3.2.2) derived from LIDAR data.

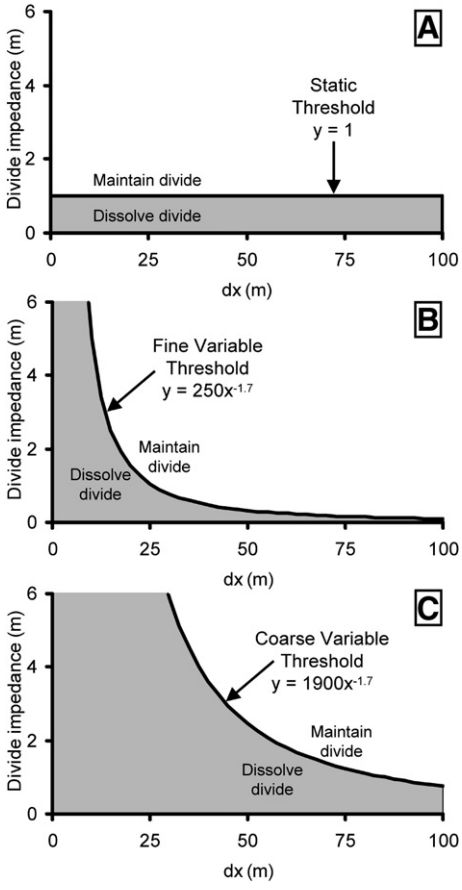


**Fig. 8.** Graphical representation of the (A) constant threshold; (B) fine variable threshold; and (C) coarse variable threshold. *x* axis values ($d_x$) are proportional to the size of the smaller of the two facets separated by any particular divide (Eq. (3)).

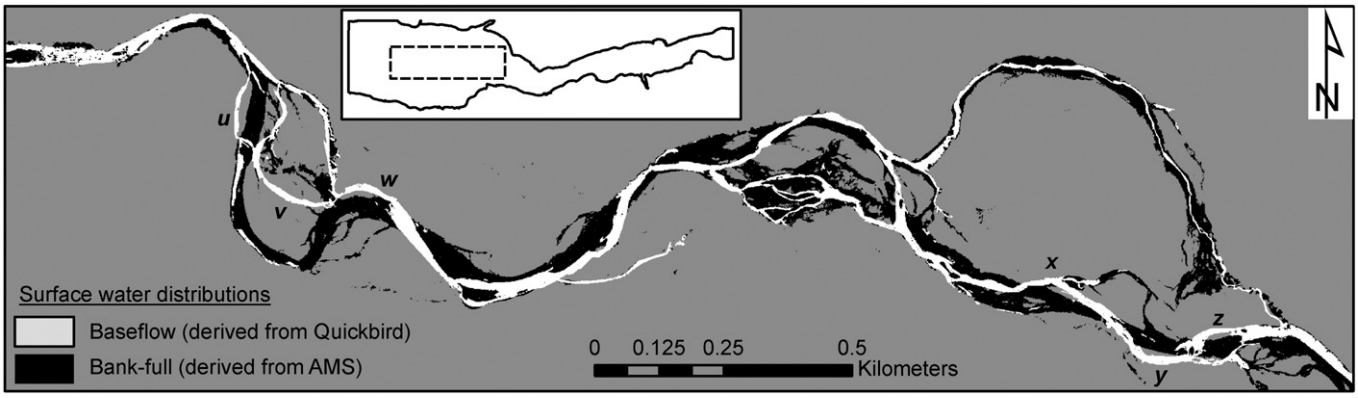


**Fig. 9.** Channel patterns at bank-full (derived from AMS data, 2003) and baseflow (derived from Quickbird data, 2004) river discharges. Note that points of disagreement (e.g., those labeled *u–z*) resulted from channel migration that occurred during intervening peak flows between the two overflight dates (see Fig. 3).

were deleted from the water mask manually based on photo-interpretation and field observations. Within the water mask, measured water depths along the river were used to create a supervised classification of water depth with the same bands from the Quickbird data set, yielding a RMSE in depth of 0.14 m. Depth data for the supervised classification were obtained by wading the river and using a stadia rod to measure channel cross sections at 41 locations, distributed approximately every 1 km along the river. Depth data were collected during the first week of August, 2004, when the river surface elevation (0.76 m gauge height) was similar to conditions captured in the Quickbird data (0.85 m gauge height). We extracted our study site from the resulting water depth grid, and subtracted the depth values from elevations in the wet-floodplain DEM, producing the dry-floodplain DEM. Differences in river stage between field data collection and Quickbird data capture likely yielded a slight (~0.1 m) bias in predicted depth values; resulting channel elevation values in the dry-floodplain DEM were therefore overestimated by a similar magnitude. We made no effort to correct for the bias because differences in stage vary spatially with channel morphology, and because the magnitude of the bias was small relative to floodplain relief.

### 3.2.2. Quantifying floodplain elevation relative to river stage

On floodplains, the water surface is sloped downstream, imparting bias to the calculation of hydrologic impedance (HI) (Fig. 5A–B), requiring that the floodplain be detrended (i.e., the effect of river gradient removed). This is sometimes accomplished by determining the best-fit plane through the floodplain surface and subtracting that plane from the floodplain DEM. However, such an approach fails to consider that the longitudinal profile of a river is not planer (Fig. 6). Instead, channel elevation is lost in "steps" as the active main channel encounters repeating patterns in bed slope variation along the floodplain. To capture the hydrologic influence of local variation in channel slope, a floodplain DEM can also be detrended by plotting the elevation of the floodplain relative to river stage (sensu Townsend & Walsh, 1998; Poole et al., 2002; Lorang et al., 2005).

To quantify the elevation of the floodplain surface relative to river stage, we used the wet-floodplain DEM to determine river stage every 5 m along the main channel, yielding 2937 estimates of main channel water stage. From these estimates, we extrapolated river stage data across the entire floodplain at 5-m resolution by applying an inverse distance weighting algorithm. To run the algorithm, we used a large distance weighting exponent (4.0) to ensure that extrapolated river stage near the river was heavily weighted by local river stage, and a large neighborhood (the 400 nearest points) so that floodplain points far from the river were assigned stage values derived from a more general trend in river stage (for more details on this rationale, see Fig. 3 in Poole et al., 2002). We used bilinear resampling to convert the extrapolated river stage map back to 1-m resolution (to match the floodplain DEM) and subtracted the extrapolated river stages from the dry-floodplain DEM, yielding a map of floodplain elevation relative to river stage. The resulting "digital relative elevation model" (DREM) provided the basis for assessing hydrologic impedance of divides among facets across the floodplain. Although the rationale underlying this analysis is identical to that presented by Poole et al. (2002), our implementation is designed for use with raster (rather than vector) GIS data sets and is also more accessible, being based on standard (rather than custom-built) GIS processing tools.

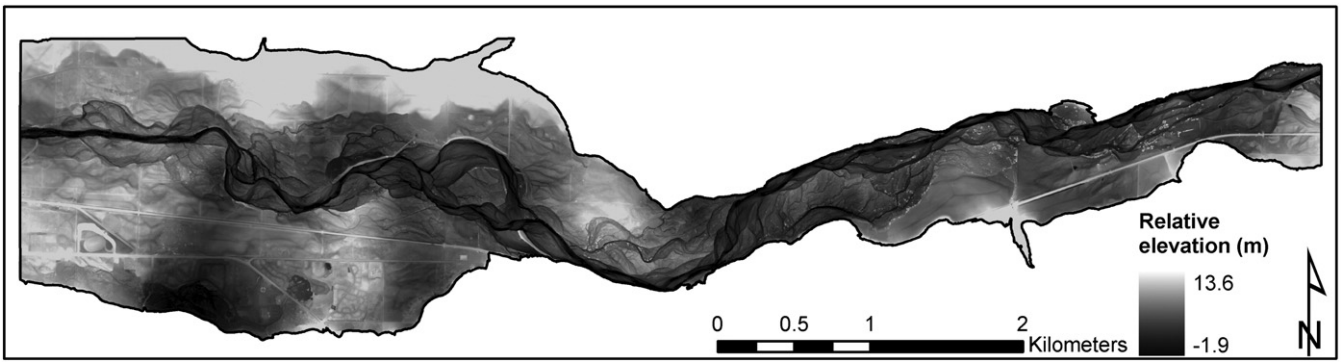


**Fig. 10.** Digital relative elevation model (DREM) showing elevation of floodplain relative to baseflow water surface elevation (see Section 3.2 for details).

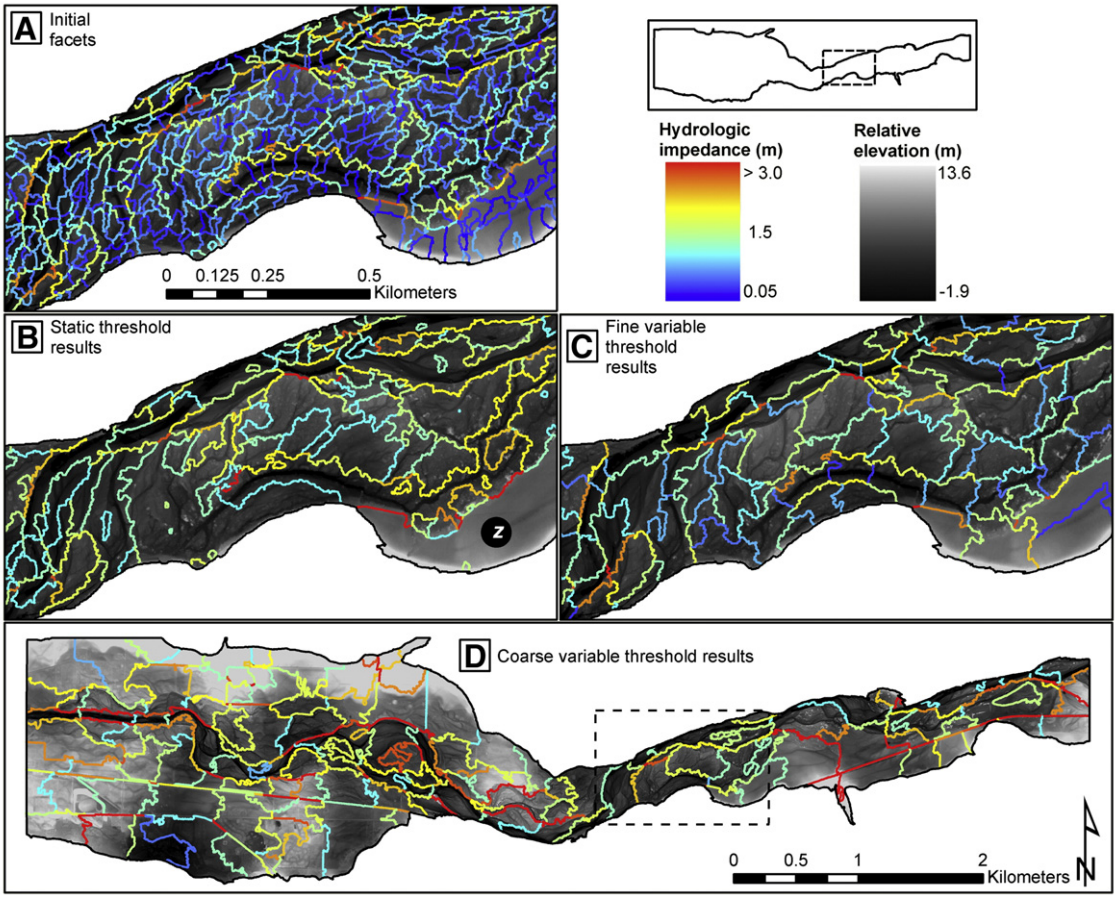


**Fig. 11.** Spatial distribution of hydrologic impedance values of divides associated with: (A) Initial facets; (B) Static threshold results; (C) Fine variable threshold results (parameters, Fig. 8B); and (D) Coarse variable threshold results (parameters, Fig. 8C). Only part of the study area is shown in A–C; inset in D shows location of A–C.

### 3.3. Delineating divides and aggregating facets

Having created the DREM, our goal was to identify a collection of hydrologic facets that represented the most significant topographic controls on surface water flux across the floodplain (i.e., facets that were bounded by divides with the highest hydrologic impedance). We developed an analysis framework (Fig. 7) which:

1) identified an initial set of hydrologic facets and associated divides from the DREM where the average facet surface area was more than an order of magnitude smaller than the facet size we ultimately desired; and
2) iteratively: a) calculated hydrologic impedance for divides; and b) aggregated pairs of facets by dissolving the divide with the lowest hydrologic impedance on the floodplain until all divides lower than a user-defined threshold were dissolved.

#### 3.3.1. Identifying initial facets and divides

To begin our analysis, we applied the ArcGIS 9.1 "Flow Direction" and "Sink" tools to identify all sinks (depressions) in the DREM ($n$=17,588). The Flow Direction tool uses a simple "D8" drainage direction algorithm, where each cell in the resulting flow-direction grid is assigned one of the 8 ordinal or subordinal flow directions; each cell on the resulting grid references the neighboring cell into which it drains. Identification of sinks is a critical first step in our analysis, but could be accomplished with essentially any flow direction algorithm (e.g., those reviewed by Erskine et al., 2006). We chose the D8 algorithm for speed and simplicity.

We filtered the sink locations to identify the lowest elevation sinks in the DREM that were spaced at least 25 m from one another ($n$=5936). We then converted the elevation of each filtered sink to "no data," thereby creating a point of internal drainage within the DREM. Using standard GIS hydrology tools for identifying drainage basins (in this case, the ArcGIS 9.1 "Fill" and "Basin" tools), we determined the

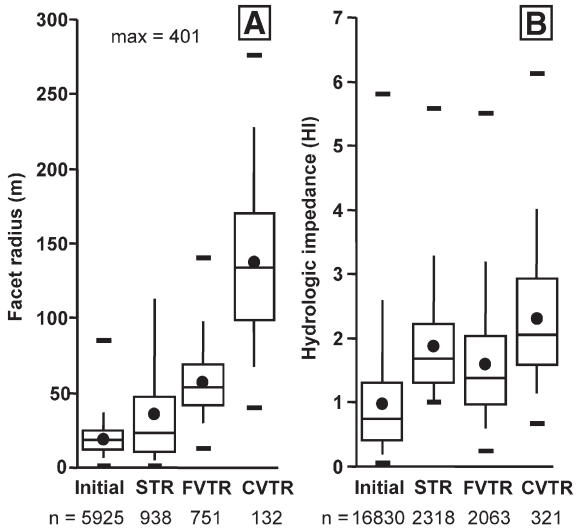


**Fig. 12.** Distributions of (A) facet radii; and (B) hydrologic impedance (HI) values for initial floodplain facets (Initial), static threshold results (STR), fine variable threshold results (FVTR), and coarse variable threshold results (CVTR). Points denote means. Box centerlines indicate medians and boxes indicate the 25th to 75th percentiles. Vertical lines denote the 5th to 95th percentiles. Horizontal bars represent minimum and maximum values.

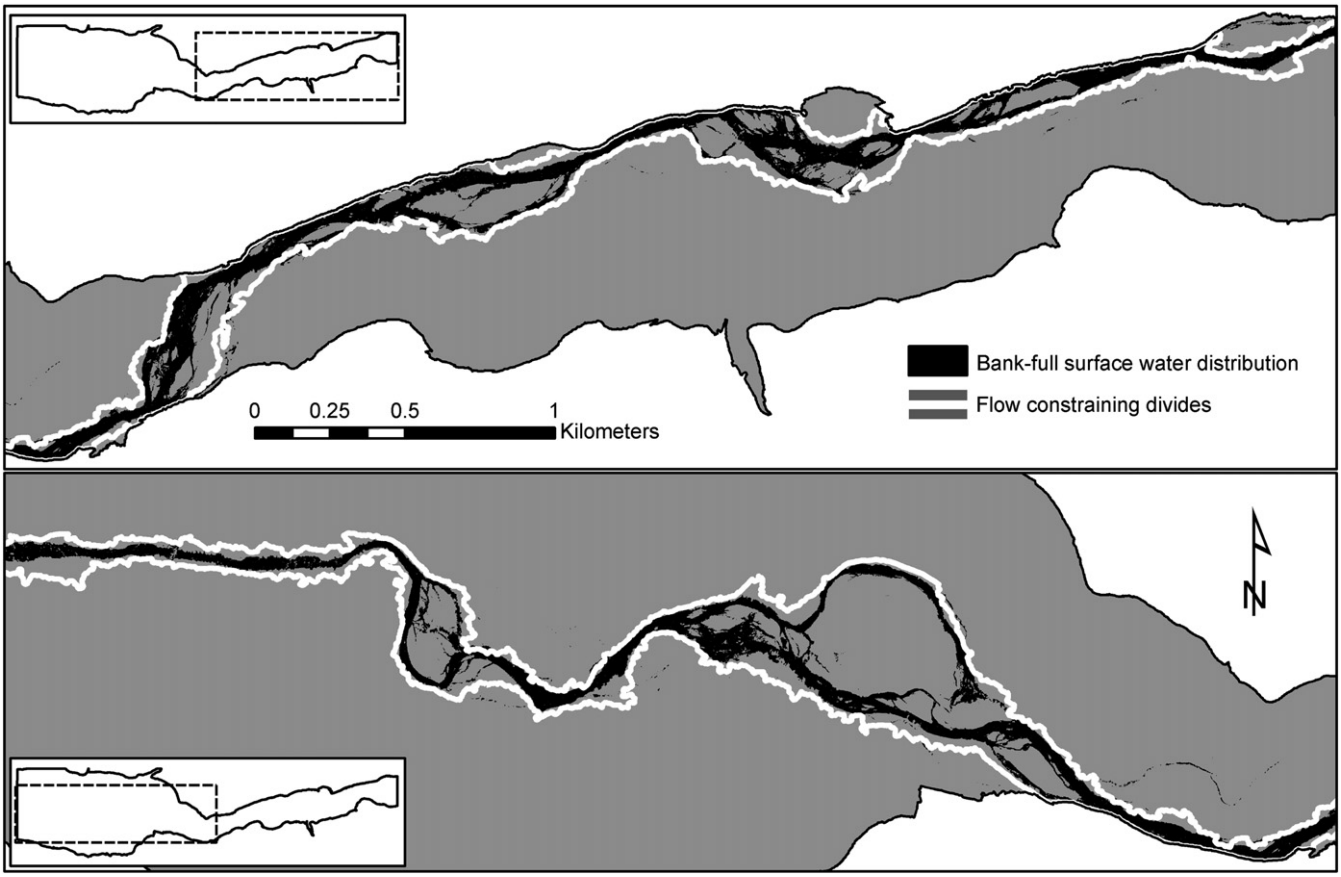


**Fig. 13.** Juxtaposition of bank-full surface water distribution (derived from AMS data) and flow-constraining divides (derived using least-cost path analysis on facet boundaries).

shape and extent of the area draining to each of the filtered sinks. We refer to the resulting drainage areas (averaging 1484 $m^2$ in area) as "initial facets" because they serve as the starting point for our aggregation analysis (described next). The boundary separating each pair of adjacent facets was identified as a distinct divide. Hydrologic impedance (HI) of each divide was then calculated according to Eq. (1).

*3.3.2. Aggregating facets*

Aggregating the initial facets into larger hydrologic facets (e.g., Fig. 1) required the strategic dissolution of divides; divides with the lowest impedance were dissolved first. We developed an ArcView Avenue script (the "aggregation script") that ranked divides by impedance values, identified the lowest impedance divide that fell below a user-defined dissolution threshold, dissolved the divide (thereby merging the two associated facets into a single larger hydrologic facet), and recalculated impedance values for all divides surrounding the newly created (merged) facet. The script continued this process until all remaining divides exceeded the dissolution threshold (Fig. 7). We ran the aggregation script three times; each run had a different method for determining the dissolution threshold.

This first run of the script used a "static threshold" of 1 m (Fig. 8A). All boundaries with a HI value <1 m were dissolved iteratively, starting with the lowest impedance boundary. The script stopped when all remaining boundaries had HI values >1 m. The application of a static threshold created a collection of aggregated facets with high variance in facet size and a non-uniform spatial distribution of facet centroids across the DREM (see Results). Throughout the remainder of this paper, we refer to this collection of facets as the "static threshold results."

While the static threshold results may be useful for some applications, our application was to parameterize a hydrologic model and, thus, required more uniform facet sizes and a more even spatial distribution of facet centroids (see Discussion). Therefore, we also created and applied a "variable threshold" in the second and third runs of the aggregation script. This threshold varied so that divides associated with small facets were more likely to be dissolved than divides associated with large facets (Fig. 8B–C). In other words, divides with somewhat higher HI values might be dissolved if they separated small facets while divides with lower HI values might not be dissolved if they separated large facets.

Applying a variable threshold required that a unique threshold value be recalculated for divides while the aggregation script was executing, based on the ever-increasing size of the associated facets. Divides were dissolved if their HI values were less than their unique threshold value. To calculate the unique threshold value for a divide, the approximate radius ($r_x$) of both associated facets was estimated from facet surface area by assuming each facet was round:

$$r_x = (A_x/\pi)^{0.5} \tag{2}$$

where $A_x$ is the surface area for facet $x$. The distance ($D$) between the centroids of the two facets was determined and apportioned among the two facets according to the ratio of facet radii, yielding an estimate of the fraction ($d_x$) of $D$ associated with each facet:

$$d_x = D \cdot r_x/(r_1 + r_2) \tag{3}$$

Using the smaller value for $d_x$ (i.e., the fraction of $D$ associated with the smaller facet), the variable impedance threshold ($T$) was calculated using a power function:

$$T = a \cdot \min(d_1, d_2)^b \tag{4}$$

where $a$ and $b$ are user-defined parameters used to determine the relationship between threshold value and $d_x$ (e.g., Fig. 8B–C). Thus,

using a variable threshold, the aggregation algorithm iteratively dissolved the divide with the lowest HI value found within the collection of divides having impedance values less than their unique value of *T*. This process is continued until no divide has a HI value less than its unique *T* value.

We applied the variable threshold approach using two different parameter sets (*a*, *b* value pairs). Using $a=250$ and $b=-1.7$ (Fig. 8B) resulted in a collection of floodplain facets with an average extent of ≈10,300 $m^2$ (the "fine variable threshold results"). Using $a=1900$ and $b=-1.7$ (Fig. 8C) yielded a collection of floodplain facets with an average extent of ≈58,800 $m^2$ (the "coarse variable threshold results").

### 3.4. Assessing output

In order to verify that our assessment identified hydrologically meaningful facet boundaries, we determined whether divides with high hydrologic impedance represented geomorphic features that constrained observed patterns of surface water routing across the floodplain. If our measure of HI is hydrologically meaningful, the HI values of divides associated with the water margins should be significantly higher than the remainder of the divides on the floodplain. Because the DREM was created using the baseflow distribution of water depths derived from Quickbird data, the DREM (and thus our assessment) was not independent of this baseflow water mask. Thus, verification of our approach required a second water mask at a different water stage. We verified our analysis by: 1) determining the bank-full surface water distribution using remote sensing data collected during an approximate bank-full flow event; 2) identifying the facet boundaries (divides) most closely associated with the margins of the new water mask; and 3) statistically comparing the HI values of these divides against the HI values of remaining floodplain divides.

#### 3.4.1. Determining the bank-full water mask

We created the bank-full surface water inundation mask at a river discharge of 77 $m^3/s$ (approximate bank-full conditions) denoted as "AMS" in Fig. 3. This mask was derived from surface temperature data collected on 3/12/2003, from 20:30 to 21:15 GMT using a Daedalus Airborne Multispectral Scanner built by SenSyTech Inc. (now Argon ST, Ann Arbor, MI). The AMS sensor had a 1.25 mrad instantaneous field of view (IFOV), resulting in a nominal spatial resolution of 1.1 m. Imagery was collected using a sensor array 1440 pixels wide with spectral ranges of 0.52–0.60, 0.76–0.90 and 8.5–12.5 μm at 12-bit radiometric quantization. Optical data remained in digital numbers (DNs). We converted thermal data to degrees Celsius by applying Planck's law to calculate the radiant temperature leaving the water surface. The calculation included a constant emissivity for water (0.97) and a simplified radiative transfer model to accommodate the low elevation (522 m AGL) of the data collection flight. AMS data were registered to the 2004 Quickbird image with a RMSE of 1.3 m. To determine the bank-full water surface from the AMS data, we used a parallelepiped classification (Jensen, 2007) with all three AMS bands based on a training set of 25,956 pixels chosen from the center of the river channel. The classification was further trained using a standard deviation of +/−2 and mean thermal and DN values. Channel patterns and forms were similar between the resulting bank-full water surface and baseflow water surface, with deviations only where channel position changed between 2003 and 2004 (Fig. 9).

#### 3.4.2. Identifying divides associated with bank-full water surface

To identify divides associated with the bank-full channel margin, we first extracted the northern and southern channel margins of the contiguous portion of the bank-full water mask. Next, we used a least-cost path analysis through the network of divides to identify the collection of divides that most closely mimicked the shape of the wetted channel margin, and thus represented the geomorphic features that were actively constraining surface water routing at bank-full flow (the "flow-constraining divides"). To accomplish this, the least-cost path analysis used a cost surface calculated as Euclidean distance (m) from the channel margin for any pixel outside the channel margins. Between the channel margins, the cost surface was set to the square of the distance from the channel margin, discouraging the least-cost path algorithm from selecting a path that crossed wetted areas of the floodplain. We compared the HI values of the flow-constraining divides to the HI values of remaining floodplain divides using a Mann–Whitney *U* Test (SPSS for Windows v.9.0.1, SPSS Inc.) to determine whether divides with high HI values were apt to be those that constrain water flow.

## 4. Results

The DREM showed that the elevation of the floodplain relative to the baseflow main channel stage averaged +2.3 m and ranged from −1.9 m within the main channel to +13.6 m on the higher portions of the floodplain (Fig. 10).

Our identification of initial facets from the DREM yielded 5925 facets and 16,830 divides across the ~8.8 $km^2$ study site (Fig. 11A). The size of these initial facets averaged 1484 $m^2$ and ranged from 10 $m^2$ to 22,652 $m^2$, yielding the distribution of estimated patch radii (*r* in Eq. (2)) shown in Fig. 12A. As would be expected, aggregation of facets reduced the number of facets and increased facet size (Fig. 11B–D), but these patterns varied depending on the threshold applied (Fig. 12A).

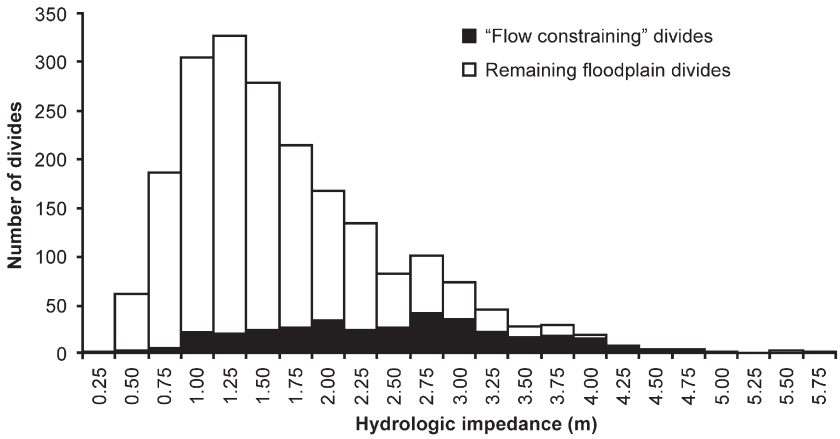


**Fig. 14.** Distributions of hydrologic impedance values along flow-constraining divides (Fig. 13) vs. all other floodplain divides. Impedance values between the two populations were significantly different ($p<0.001$, Mann–Whitney *U* Test).

Application of a static threshold (1 m) had little effect on the lower end of the size distribution, but markedly stretched the upper end of the distribution ("STR," Fig. 12A). In contrast, application of a variable threshold increased the lower, central, and upper portion of the size distribution and, as intended, normalized the size distribution by reducing the initial skew toward smaller size classes ("FVTR" and "CVTR," Fig. 12A).

HI values for divides associated with the initial facets ranged from 0.05 m to 5.8 m with a mean of 0.97 m (Fig. 12B). Since divides with lower HI values were dissolved preferentially, application of both static and variable thresholds yielded an upward shift in the lower end and central tendency of the HI distributions. Changes in maximum HI values, however, did not respond consistently. Surprisingly, dissolving boundaries with low hydrologic impedance can either decrease or increase the maximum hydrologic impedance values on the floodplain. Although no change in maximum values might be expected from dissolving only low-impedance boundaries, various patterns of juxtaposition among facets will result in an indirect loss of boundaries with high-impedance values or an indirect increase in the impedance values of remaining adjacent boundaries when low-impedance boundaries are removed (see Discussion).

As intended, the overall pattern of the flow-constraining divides, identified by least-cost path analysis, closely conformed to the shape of the north and south channel margins (Fig. 13). HI values of these flow-constraining divides were significantly higher than the remaining floodplain divides (Fig. 14; $p<0.001$, Mann–Whitney $U$ Test), suggesting that our assessment based on hydrologic impedance effectively identified the geomorphic features constraining the observed bank-full distribution of surface water.

## 5. Discussion

Changes in the distributions of facet size and divide impedance resulting from facet aggregation (Fig. 12A–B) generally conformed to our expectations. Application of a static threshold yielded a substantive increase in facet size variability because of spatial clustering of similar HI values on the floodplain. The floodplain contains large, contiguous areas that lack divides with high hydrologic impedance. When boundaries are dissolved using a static threshold, such areas are merged into a single, large facet (e.g., the large facet labeled "z" in Fig. 11B resulted from an area with uniformly low HI, shown in Fig. 11A). Similarly, some very small facets are occasionally bounded by divides with high hydrologic impedance and, thus, remain as independent facets after applying the static threshold (Fig. 11B). By design, the variable threshold yielded a more uniform and normal distribution of facet sizes than a static threshold (Figs. 11C–D and 12A) because, under the variable threshold, boundaries separating small facets are more likely to be dissolved than those separating large facets (Fig. 8).

Some changes in the distribution of facet sizes, however, were less intuitive. Our iterative approach to dissolving boundaries will not yield the same distribution of hydrologic impedances across the floodplain as would be derived from identifying all of the initial divides with HI values below a given threshold and dissolving those divides simultaneously. The latter approach would truncate the original distribution of HI values and would not result in a set of facets that optimally represents the floodplain surface. An optimal solution was obtained with our iterative approach because the distribution of HI values evolved during the analysis via a number of interactions among facets that are not initially obvious. For instance, when a single divide was dissolved, the arrangement of remaining adjacent divides and their associated HI values may change (Fig. 15). Although only low-impedance divides were removed directly, the indirect effects of dissolving a divide sometimes resulted in a loss of adjacent divides with high HI values or yielded an increase in HI values of adjacent divides. Thus, the upper end of the frequency distribution of HI values is also affected indirectly (e.g., changes in maximum HI values shown in Fig. 12B).

Under all scenarios, high-impedance values tended to cluster spatially in or near the active scour zone of the channel and along key natural and man-made geomorphic features such as cut banks, roads, levees, etc. (Fig. 11A–D). Results from the least-cost path analysis (Fig. 14) provided statistical confirmation of the visual patterns of spatial correlation among high-impedance divides and the observed channel margin (Fig. 13), suggesting that our measure of HI is useful for ranking the potential influence of geomorphic features on surface water hydrology. Given that HI measured the change in stage necessary to overtop a geomorphic feature (Fig. 4), the mechanism behind this strong spatial correlation is straightforward. When river stage rises, only a small change in stage will be necessary to overtop features with low impedance, meaning that these features will define the channel margin for only a small range of river stages. However, features with high impedance will continue to constrain the channel margin even over large changes in river stage. Thus, features with high HI are most likely to define the channel margin at any given river stage.

### 5.1. Applications

We have presented static and variable thresholds as a simple contrast in rules one might use to tailor the process of dissolving

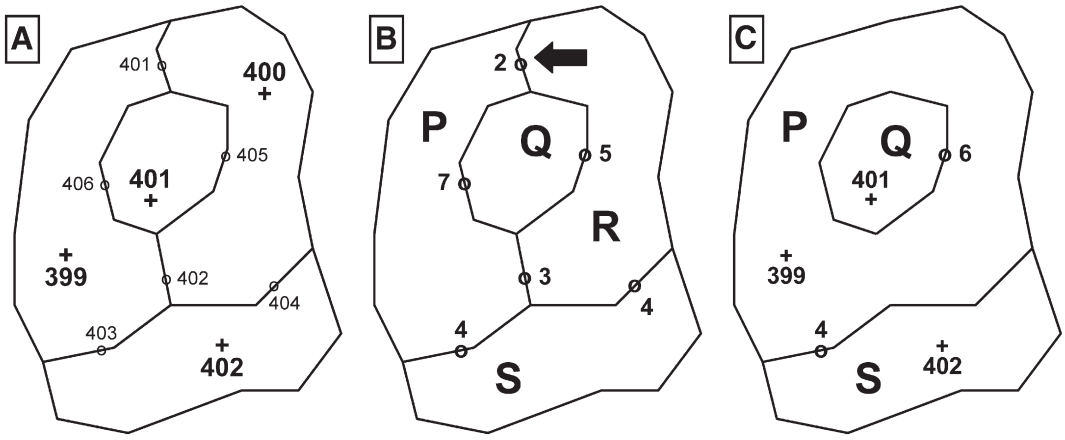


**Fig. 15.** Direct and indirect effects of dissolving a single divide within a hypothetical configuration of hydrologic facets. (A) Elevation of lowest points within four adjacent facets and along six associated divides. (B) Hydrologic impedance of divides calculated according to Eq. (1). The divide with the lowest impedance (upper boundary P–R, indicated by arrow) will be dissolved directly. Indirect effects include: loss of lower divide P–R (because R merges into P to form a single facet); joining of divide P–S with R–S; joining of divide P–Q with Q–R; and a change in the impedance value originally associated with divide Q–R. (C) Resulting configuration of facets and divides, with associated impedance values after dissolving a single divide.

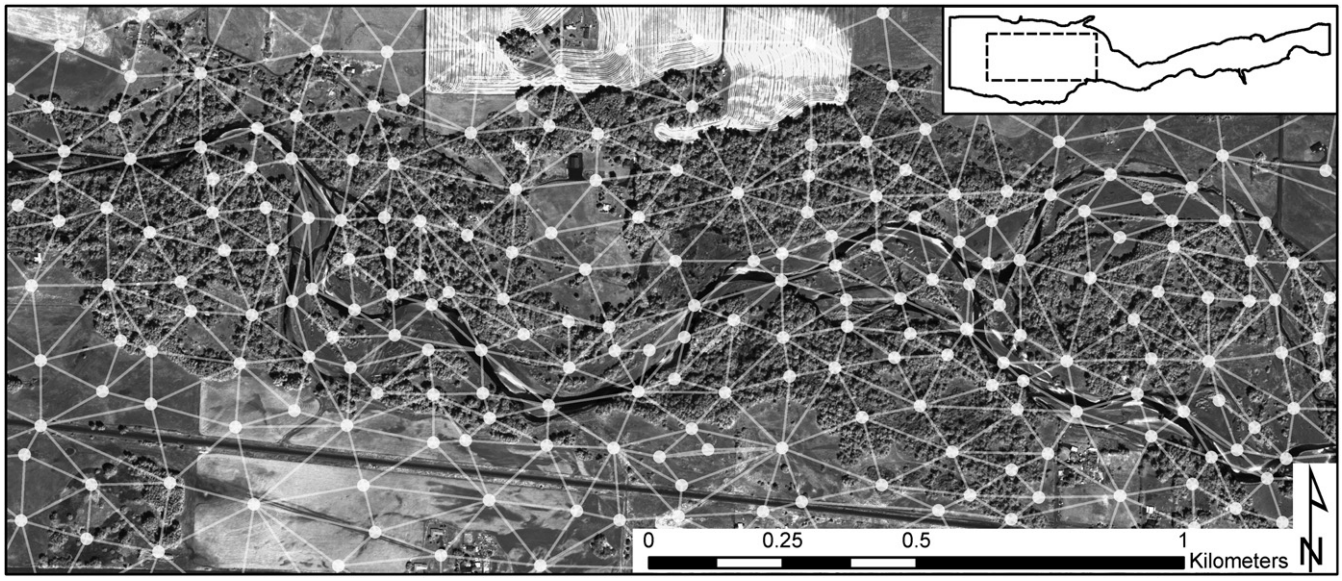


**Fig. 16.** Link-and-node flow network derived from the fine variable threshold results. Such a flow network can be used to parameterize a dynamic hydrologic model of surface water flux across the floodplain.

divides. While they represented an interesting contrast, both static and variable thresholds have associated potential for real-world applications.

A static threshold will identify divides that are most influential on surface water routing across a low-relief fluvial landscape. Absolute elevations and locations of these divides can be extracted from a LIDAR dataset to provide a simplified representation of geomorphic controls on surface water hydrology that would allow computationally efficient assessment of patterns of surface water connection at various river stages. These patterns could be applied in both ecological assessments (e.g., habitat mapping) and regulatory analyses (e.g., establishing a 100-year floodplain for zoning purposes).

The variable threshold approach is useful in applications where a more uniform distribution of facets is desirable. Specifically, we designed our variable threshold to create surface water flow networks with node and link locations optimized to represent topographic controls on surface water movement, while still spacing nodes evenly across the analysis area (Fig. 16). These networks provide the basis for finite volume link-and-node modeling approaches to simulating water flux atop the floodplain surface (Walton et al., 1996; Poole et al., 2004). Unlike hillslope modeling approaches, link-and-node modeling approaches are well suited to simulating dynamic flow conditions such as bidirectional flows, converging and diverging flow paths, and expansion and contraction of flow networks. Additionally, such models can be linked to hydrogeologic models to describe complex patterns of ground and surface water exchange on floodplain (Poole et al., 2006).

To describe a flux network representing a geomorphic surface (e.g., Fig. 16) within our link-and-node model (Poole et al., 2004; Poole et al., 2006), we use facet characteristics to parameterize model nodes and characteristics of divides to parameterize links. For instance, during a simulation, the model tracks changes in the volume of water associated with each model node (i.e., within each floodplain facet). The model then uses water volume to estimate water surface elevation and inundation area at each node (i.e., within each floodplain facet). Because the high-resolution DEM can be used to generate a precise elevation distribution within each facet, the resulting precise relationship between water volume and stage or inundated area can be used to parameterize each model node. Similarly, water flux rates within model links are dependent upon the bed elevation and channel cross-section. These parameters can be derived directly from the elevation distribution traced along facet divides. In the absence of a map of hydrologic facets, such parameters for links and nodes are derived based on arbitrary node locations and assumptions such as prismic channel cross sections (sensu Walton et al., 1996; Poole et al., 2004). Thus, rather than use arbitrary grids or triangulated networks to parameterize the model, our strategic algorithm for simplifying LIDAR topographic data optimizes the representation of geomorphic controls on floodplain hydrology given a desired number of links and nodes in the model, and, therefore, will maximize model accuracy.

Our method has at least two important limitations. First, the accuracy of the DEM is limited by LIDAR technology. For instance, LIDAR echoes from the top of low vegetation can be misclassified as ground surface returns. Resulting errors in a DEM will yield mischaracterization of hydrologic impedance and will yield inaccuracies in any subsequent hydrologic model. Fortunately, LIDAR sensors provide the entire backscattered waveform (rather than just first and last echoes), allowing improved classification of terrain and off-terrain points and yielding DEMs with higher accuracy. Second, while our methodology cannot rectify some problems common in LIDAR-based simulations of surface water hydrology (e.g., roads and bridges identified as flow barriers, sensu Barber & Shortridge, 2004, 2005), model links within our finite volume hydrologic model can be parameterized to represent a variety of hydrologic control structures, e.g., a culvert or weir (Walton et al., 1995) when information on the location of such hydraulic structures is available to augment the LIDAR data.

## 6. Conclusions

LIDAR data yield high-resolution DEMs of low-relief fluvial landscapes. Associated hydrologic assessment of these landscapes, however, may benefit from abandoning the typical assumptions underlying hydrologic analysis of DEMs (e.g., continual convergence of flow and drainage to the edge of the landscape). Our alternative approach, based on patterns of surface water connectivity among adjacent depressions, uses the concept of hydrologic impedance to identify geomorphic features (i.e., divides) that constrain and shape patterns of surface water flux and routing. Using this method, the geomorphic detail provided by LIDAR data can be simplified automatically and strategically via an optimal aggregation of depressions into asymmetric yet hydrologically meaningful landscape facets according to user-defined aggregation criteria. Such an analysis can

facilitate efficient hydrological assessments and parameterization of simulation models to investigate surface water flux on floodplains and other fluvial landscapes.

## Acknowledgements

Ned Gardiner originally envisioned a spatial comparison between HI values and observed bank-full surface water distributions be included in this paper. Jan-Olaf Meynecke provided constructive review of a pre-submission draft. Comments from Ned Gardiner and two anonymous reviewers also helped to improve this work. Funding was provided by grants from the National Research Initiative of the USDA Cooperative State Research, Education, and Extension Service, Grant # 2005-35102-16288 and from the National Science Foundation (EAR-0120523), with additional support from Bonneville Power Administration (200725200) and NASA (NAG13-02030).

## References

Barber, C. P., & Shortridge, A. M. (2004). *Light detection and ranging (LiDAR)-derived elevation for surface hydrology applications* (p. 11). East Lansing, MI: Institute of Water Research, Michigan State University.

Barber, C. P., & Shortridge, A. M. (2005). Lidar elevation data for surface hydrologic modeling: Resolution and representation issues. *Cartography and Geographic Information Science*, *32*, 401–410.

Bates, P. D., Marks, K. J., & Horritt, M. S. (2003). Optimal use of high-resolution topographic data in flood inundation models. *Hydrological Processes*, *17*, 537–557.

Byrd, K. B., & Kelly, M. (2006). Salt marsh vegetation response to edaphic and topographic changes from upland sedimentation in a Pacific estuary. *Wetlands*, *26*, 813–829.

Casas, A., Benito, G., Thorndycraft, V. R., & Rico, M. (2006). The topographic data source of digital terrain models as a key element in the accuracy of hydraulic flood modeling. *Earth Surface Processes and Landforms*, *31*, 444–456.

Charlton, M. E., Large, A. R. G., & Fuller, I. C. (2003). Application of airborne LiDAR in river environments: The River Coquet, Northumberland, UK. *Earth Surface Processes and Landforms*, *28*, 299–306.

Erskine, R. H., Green, T. R., Ramirez, J. A., & MacDonald, L. H. (2006). Comparison of grid-based algorithms for computing upslope contributing area. *Water Resources Research*, *42*, W09416.

Florsheim, J. L., & Mount, J. F. (2002). Restoration of floodplain topography by sand–splay complex formation in response to intentional levee breaches, Lower Cosumnes River, California. *Geomorphology*, *44*, 67–94.

Fonda, R. W. (1974). Forest succession in relation to river terrace development in Olympic National Park, Washington. *Ecology*, *55*, 927–942.

Gurnell, A. M., van Oosterhout, M. P., de Vlieger, B., & Goodson, J. M. (2006). Reach-scale interactions between aquatic plants and physical habitat: River Frome, Dorset. *River Research and Applications*, *22*, 667–680.

Jensen, J. R. (2007). *Remote sensing of the environment: An earth resource perspective.* Upper Saddle River, NJ: Prentice Hall.

Jenson, S. K. (1991). Applications of hydrologic information automatically extracted from digital elevation models. *Hydrological Processes*, *5*, 31–44.

Jenson, S. K., & Domingue, J. O. (1988). Extracting topographic structure from digital elevation data for geographic information-system analysis. *Photogrammetric Engineering and Remote Sensing*, *54*, 1593–1600.

Jones, K. L., Poole, G. C., Woessner, W. W., Vitale, M. V., Boer, B. R., O'Daniel, S. J., Thomas, S. A., & Geffen, B. A. (2008). Geomorphology, hydrology, and aquatic vegetation drive seasonal hyporheic flow patterns across a gravel-dominated floodplain. *Hydrological Processes*, *22*, 2105–2113.

Junk, W. J., Bayley, P. B., & Sparks, R. E. (1989). The flood pulse concept in river-floodplain system. *Canadian Special Publication of Fisheries and Aquatic Sciences*, *106*, 110–127.

Kondolf, G. M., Boulton, A. J., O'Daniel, S., Poole, G. C., Rachel, F. J., Stanley, E. H., et al. (2006). Process-based ecological river restoration: Visualizing three-dimensional connectivity and dynamic vectors to recover lost linkages. *Ecology and Society*, *11*, 5.

Lane, S. N., James, T. D., Pritchard, H., & Saunders, M. (2003). Photogrammetric and laser altimetric reconstruction of water levels for extreme flood event analysis. *Photogrammetric Record*, *18*, 293–307.

Leopold, L. B., Wolman, M. G., & Miller, J. P. (1964). *Fluvial processes in geomorphology.* San Francisco: W.H. Freeman and Co.

Lohani, B., & Mason, D. C. (2001). Application of airborne scanning laser altimetry to the study of tidal channel geomorphology. *ISPRS Journal of Photogrammetry and Remote Sensing*, *56*, 100–120.

Lorang, M. S., Whited, D. C., Hauer, F. R., Kimball, J. S., & Stanford, J. A. (2005). Using airborne multispectral imagery to evaluate geomorphic work across floodplains of gravel-bed rivers. *Ecological Applications*, *15*, 1209–1222.

Maidment, D. (2002). *ArcHydro: GIS for water resources.* Redlands, CA: ESRI Press.

Malanson, G. P., & Butler, D. R. (1991). Floristic variation among gravel bars in a subalpine river, Montana, U.S.A.. *Arctic and Alpine Research*, *23*, 273–278.

Malard, F., Tockner, K., & Ward, J. V. (1999). Shifting dominance of subcatchment water sources and flow paths in a glacial floodplain, Val Roseg, Switzerland. *Arctic, Antarctic, and Alpine Research*, *31*, 135–150.

Mason, D. C., Scott, T. R., & Wang, H. J. (2006). Extraction of tidal channel networks from airborne scanning laser altimetry. *ISPRS Journal of Photogrammetry and Remote Sensing*, *61*, 67–83.

Omer, C. R., Nelson, E. J., & Zundel, A. K. (2003). Impact of varied data resolution on hydraulic modeling and floodplain delineation. *Journal of the American Water Resources Association*, *39*, 467–475.

Poole, G. C., Stanford, J. A., Frissell, C. A., & Running, S. W. (2002). Three-dimensional mapping of geomorphic controls on flood-plain hydrology and connectivity from aerial photos. *Geomorphology*, *48*, 329–347.

Poole, G. C., Stanford, J. A., Running, S. W., & Frissell, C. A. (2006). Multi-scale geomorphic drivers of ground-water flow path dynamics: Subsurface hydrologic dynamics and hyporheic habitat diversity. *Journal of the North American Benthological Society*, *25*, 288–303.

Poole, G. C., Stanford, J. A., Running, S. W., Frissell, C. A., Woessner, W. W., & Ellis, B. K. (2004). A patch hierarchy approach to modeling surface and sub-surface hydrology in complex flood-plain environments. *Earth Surface Processes and Landforms*, *29*, 1259–1274.

Pringle, C. M. (2003a). The need for a more predictive understanding of hydrologic connectivity. *Aquatic Conservation-Marine and Freshwater Ecosystems*, *13*, 467–471.

Pringle, C. M. (2003b). What is hydrologic connectivity and why is it ecologically important? *Hydrological Processes*, *17*, 2685–2689.

Townsend, P. A., & Walsh, S. J. (1998). Modeling floodplain inundation using an integrated GIS with radar and optical remote sensing. *Geomorphology*, *21*, 295–312.

Walton, R., Chapman, R. S., & Davis, J. E. (1996). Development and application of the wetlands dynamic water budget model. *Wetlands*, *16*, 347–357.

Walton, R., Martin, T. H., Chapman, R. S., & Davis, J. E. (1995). *Investigation of wetlands hydraulic and hydrological processes, model development, and application.* Vicksburg, MS: US Army Corps of Engineers, Waterways Experiment Station.

Wang, L., & Liu, H. (2006). An efficient method for identifying and filling surface depressions in digital elevation models for hydrologic analysis and modeling. *International Journal of Geographical Information Science*, *20*, 193–213.

Woolard, J. W., & Colby, J. D. (2002). Spatial characterization, resolution, and volumetric change of coastal dunes using airborne LIDAR: Cape Hatteras, North Carolina. *Geomorphology*, *48*, 269–287.

Zedler, J. B., Callaway, J. C., Desmond, J. S., Vivian-Smith, G., Williams, G. D., Sullivan, G., et al. (1999). Californian salt-marsh vegetation: an improved model of spatial pattern. *Ecosystems*, *2*, 19–35.